
Article:
Chechik, L. orcid.org/0000-0002-7626-2694, Christofidou, K.A. orcid.org/0000-0002-8064-5874, Markanday, J.F.S. et al. (5 more authors) (2022) Hardness variation in inconel 718 produced by laser directed energy deposition. Materialia, 26. 101643. ISSN 2589-1529

https://doi.org/10.1016/j.mtla.2022.101643

MTLA 26 (2022) 101643

Contents lists available at ScienceDirect

Materialia

journal homepage: www.elsevier.com/locate/mtla

Hardness variation in inconel 718 produced by laser directed energy deposition

Lova Chechik [a], Katerina A. Christofidou [a], Jonathon F.S. Markanday [b], Alexander D. Goodall [a], James R. Miller [b], Geoff West [c], Howard Stone [b], Iain Todd [a,*]

[a] Department of Materials Science and Engineering, The University of Sheffield, Mappin Street, S1 3JD, UK
[b] Department of Materials Science & Metallurgy, University of Cambridge, 27 Charles Babbage Road, CB3 0FS, UK
[c] Warwick Manufacturing Group (WMG), University of Warwick, Coventry, CV4 7AL, UK

ARTICLE INFO

Keywords:
Laser deposition
Precipitation
Hardness
Ni-based superalloys

ABSTRACT

Directed energy deposition (DED) of Inconel 718 is of critical importance for the repair of aerospace components, which have tight tolerances for certification, particularly on mechanical properties. Significant hardness variation has been seen throughout DED manufactured Inconel 718 components, suggestive of variation in mechanical properties, which must be understood such that the variation can either be removed, or implemented within the design in line with regulatory guidance. In this work, γ' precipitation was theorised to be the cause of hardness variation throughout the component, despite Inconel 718 conventionally being regarded as a γ" strengthened alloy. A simple precipitation potential model based on a moving heat source was found to correlate with the measured hardness and explain the hardness distribution observed. In addition, it has been shown that sections under a critical thickness of 2 mm never reach the peak hardness in the as-built condition. This understanding allows for the development of in-situ heat treatment strategies to be developed for microstructural, and hence, mechanical property optimisation, necessary for repair technologies where post processing steps are limited.

1. Introduction

Inconel 718 is a nickel superalloy widely used in critical aerospace components with operating temperatures up to 650°C [1,2]. The main strengthening mechanism is precipitation and order strengthening due to the formation of the body centred tetragonal γ", Ni_3Nb, phase [1,3–5], with a small strengthening contribution from the γ', $Ni_3(Al,Ti)$, phase. Typically, the volume fraction of γ" precipitates in cast and wrought Inconel 718 is 15-20 % [4,6] with up to 5 % γ'.

Directed energy deposition (DED) is a type of additive manufacturing (AM) method, which is widely used in the aerospace sector due to its ability to add to an existing component and be used in repair applications [7,8]. The repair of components such as turbine blisks is economically preferable to their replacement. Inconel 718 is widely regarded as the "workhorse of the aero-engine sector" [2], so DED repairs using Inconel 718 are of great industrial interest [8]. Heat treatments are typically used post AM to improve mechanical properties [2,9]; due to the complex geometries being repaired, localised heat treating of the repairs may not be possible. For this reason, using in-situ heat treatments is of great interest [4,10].

Numerous thermal studies have been performed, analysing the precipitation behaviour of Inconel 718. Often, the precipitation of γ' and γ" are analysed together due to their formation at similar temperatures [1,3]. However, as the γ" accounts for 70-80 % of all precipitates [1,11], it is believed that these studies are indeed representative of the γ" precipitation behaviour in Inconel 718. Despite Inconel 718 primarily being a γ" strengthened alloy, γ' is the first precipitate to form and then γ" precipitates form subsequently on the γ' phase, as initially hypothesised by Cozar and Pineau [12–15]. Differential scanning calorimetry (DSC) thermograms show sigmoids at temperatures where precipitation occurs. For γ', this is at around 500-650°C for conventionally processed material (seemingly lower during AM than otherwise observed), whilst for γ" this is around 700-900°C [3,16,17], the latter of which is within the short-term aging temperature range of γ'/ γ" (700-900°C) identified

Abbreviations: AM, Additive Manufacturing; DED, Directed Energy Deposition; DSC, Differential Scanning Calorimetry; EBSD, Electron Backscatter Diffraction; GAM, Grain Average Misorientation; GCP, Geometrically Close Packed; KAM, Kernel Average Misorientation; SEM, Scanning Electron Microscopy; TEM, Transmission Electron Microscopy; TTT, Time-Temperature-Transformation.

* Corresponding author.
E-mail address: iain.todd@sheffield.ac.uk (I. Todd).

https://doi.org/10.1016/j.mtla.2022.101643
Received 8 November 2022; Accepted 23 November 2022
Available online 25 November 2022

by Slama and Abdellaoui [1]. Time-Temperature-Transformation (TTT) curves for Inconel 718 show a combined γ' and γ" precipitation window with a minimum time for transformation of the order 0.1 s and sub second transformation times roughly in the temperature range of 650-900°C [3], the nose of the curve is at shorter times for γ' than for γ" [18].

Due to its wide applicability in industry as well as the age-hardenable behaviour of Inconel 718, it is particularly popular for manufacturing using additive processes. γ" is typically found in the interdendritic regions of additively manufactured (AM) samples [19], as these contain up to four times more Nb due to segregation during solidification [13] increasing the precipitation kinetics by an order of magnitude [18]. Tian *et al.* hypothesise that on initial solidification, Nb-rich eutectic products are formed interdendritically [20]. In subsequent hatches/layers, these low melting point eutectics remelt, allowing for Nb diffusion away from them, and leading to the γ" precipitation and growth [20]. Kumara *et al.* extend this argument by saying that these high Nb concentrations in the interdendritic regions form Laves phases upon solidification [18]. During subsequent hatches, Nb diffuses back out of these Laves phases and γ" forms nearby the Laves phases [18]. Interestingly, these studies do not report the occurrence of γ' precipitates, despite this normally forming before γ" precipitation.

The majority of precipitation work has been completed with the heat treatment of wrought material in mind, 720°C for 8 hours being a representative heat treatment for a γ" aging cycle [9]. Although the morphology of the precipitates in wrought and AM material may be similar, the AM process occurs at much higher speeds with cooling rates around 10^3-10^4°C/s for DED [21], with sub-second holding periods within the precipitation range. The TTT curve reaching 0.1 s suggests that precipitation could occur during DED, but this does not fully predict the precipitation kinetics. As a result of the AM process being so far from equilibrium, there is limited understanding of the precipitation reactions occurring, which explains the range of observations reported in literature.

During AM, multiple reheats occur in the subsequent hatches and layers, which would allow for more time in the precipitation temperature range. However, γ" can transform to δ at temperatures above 900°C [1,3], which is a geometrically close packed (GCP) phase and can be deleterious to mechanical performance leading to embrittlement. Despite this, it has been shown that γ" can be retained when aged samples are held at 1100°C for 1 s and subsequently cooled at 10°C/min (total of 21 mins above 900°C), no mention of γ' was included in these samples [3]. Tian et al. [20] hypothesised that more γ" was found at the bottom of an as-build DED sample which explains the decrease of hardness they observed with height. The cause of this was speculated to be due to growth and precipitation of γ" in subsequent hatches and layers as allowed by Nb segregation [20]. Hardness was shown to increase with height, but no quantification of temperature cycles to precipitation kinetics was attempted [20].

Electron beam powder bed fusion (EB-PBF) has been used to show that by holding the baseplate at high temperatures, the volume fraction of precipitates (both γ' and γ") can be increased [22]. This method was used to recreate standard heat treatments (1-8 hrs), which were shown to retain both γ' and γ". The resultant hardness values of these samples was 478±7 HV, significantly higher than samples built without the in-situ heat-treatment and comparable to those achieved in the peak aged wrought alloy [4]. In addition, 2 further cooling rates were tested, with the slower one resulting in a higher hardness, which would be expected due to the increased time in the precipitation range [4].

In addition to precipitation strengthening, the density of dislocations can be related to the yield stress using $\sigma_y \propto \sqrt{\rho}$, where ρ is the dislocation density [23,24]. The geometrically necessary dislocation density can be approximated using EBSD data [25,26]; the grain average misorientation (GAM) being reported as being proportional to the dislocation density [26,27]. There are some reports of this being an underestimate, but the trend of $\sigma_y \propto GAM$ remains [28]. The dislocation density has been shown to be proportional to yield strength in DED, showing a strength variation with build height [29].

Despite the technological importance of the material and the sustainability benefits offered by repairing components through DED, the as-built hardness heterogeneity of Inconel 718 is yet to be fully explained. Furthermore, modelling efforts to understand the precipitation kinetics of the materials under DED conditions are complex and cannot be easily employed, thus simple, empirical models of precipitation kinetics are necessary in order to guide the process and allow for the optimisation of as built components/repairs. To this end, this work explores the hardness trends in as-built DED components and further analyses the sources of hardness variation utilising advanced characterisation and simple modelling tools.

2. Experimental methods

Samples were built using Inconel 718 powder of size range 45–150 μm (supplied by LPW) produced by the plasma rotating electrode process, with composition summarised in Table 1. A BeAM Magic 2.0 DED machine was used with a 0.7 mm spot 2kW laser and 12 l/min of argon shielding gas flow. Samples were built on an Inconel 718 substrate, with the nozzle placed 3.5 mm above the substrate.

Walls of six different thicknesses (controlled by number of hatches) were built, ranging from 1 hatch (1.1 mm thickness) to 8 hatches (3.6 mm thickness) all with consistent build parameters as summarised in Table 2. These were sectioned at the midpoint in the YZ section as shown by the orange line in Fig.1a, which includes axis definitions. In addition, two triangular prisms were printed with equilateral triangular bases of length 27.5 mm; the hatching strategies were from base to tip and from tip to base, as shown schematically in Fig. 1c. These were sectioned in the YZ plane along the midpoint of the triangular section. One extra wall was built for DSC analysis; this was also sectioned in the YZ plane.

Coaxial melt pool monitoring was performed using a greyscale Basler acA1440–73gm camera, filtered to a 660-1000 nm range. Images were recorded at 75 fps using an exposure time of 4000 μs for all builds listed in Table 2. The resultant 12-bit images (500 × 500 px) were analysed in Matlab R2021b. For each image, all the pixels were summed to give an overall thermal intensity, similarly to Baraldo et al. [30]. This was compared to both the maximum intensity in a single image and to the melt pool area (calculated using an intensity threshold of 20) as seen in Supplementary Fig. 1 for the 6 hatch wall. These plots are linear at intensity sums of above 0.2×10^7 (marked by the black line), which suggests that the intensity sum (thermal intensity) can be used as a proxy of melt pool temperature/size. The images with sums below 0.2×10^7 were ignored as they indicated where the laser is off or ramping up/down at the hatch edges.

For each of the walls, one half was polished using standard metallographic preparation procedures to a 1 μm finish, these were used for hardness indentation. The other half was further polished using 0.25 μm colloidal silica for EBSD. The triangular prisms were sectioned along the orange line shown in Fig. 1a. One half had the top (XY) surface polished to a 1 μm finish and the other half had the internal YZ section polished, both for hardness indentation.

Hardness was performed using a Durascan 70 Vickers indenter with a 1 kg load, 15 s hold and the indent automatically measured using a 40x optical lens. Walls were indented with an array of indents in the YZ section, spaced 0.25 mm in the Y axis and 0.75 mm in the Z axis. Triangular prisms were indented with square arrays of 1 mm spacing in both the XY and YZ cross sections.

EBSD of the walls was performed using a Jeol 7900F with an Oxford Instruments Symmetry EBSD detector. A 3 μm step size was chosen with a 13 mm work offset and a ~ 90 nA probe current. Walls were scanned with the area covering the full thickness (Y axis) with height of 1.5 mm (Z axis). EBSD analysis was performed using MTEX 5.7.0, an open source MATLAB Toolbox [31]. Grains were calculated using a threshold grain boundary misorientation of 10°, with a minimum of 3 pixels per grain.

Table 1
Composition of Inconel 718 Powder, stated by supplier (wt.%).

Cr	Ni	Co	Mo	Nb + Ta	Ti	Al	Fe	C	B
18.72	51.85	0.03	3.0	5.12	0.80	0.52	19.91	0.05	<0.005

Table 2
Parameters used for both wall and triangular prism samples.

Sample	Wall Thickness (mm)	Power (W)	Velocity (mm/min)	Hatch Spacing (μm)	Z Step (μm)	Mass flow (g/min)
1 hatch Wall	1.1	300	2250	400	200	6-6.5
2 hatch Wall	1.3					
3 hatch Wall	1.7					
4 hatch Wall	2.1					
6 hatch Wall	2.8					
8 hatch Wall	3.6					
Base to Tip Triangular Prism	-	275	2000	350	225	6.5-7.5
Tip to Base Triangular Prism	-	275	2000	350	225	6.5-7.5

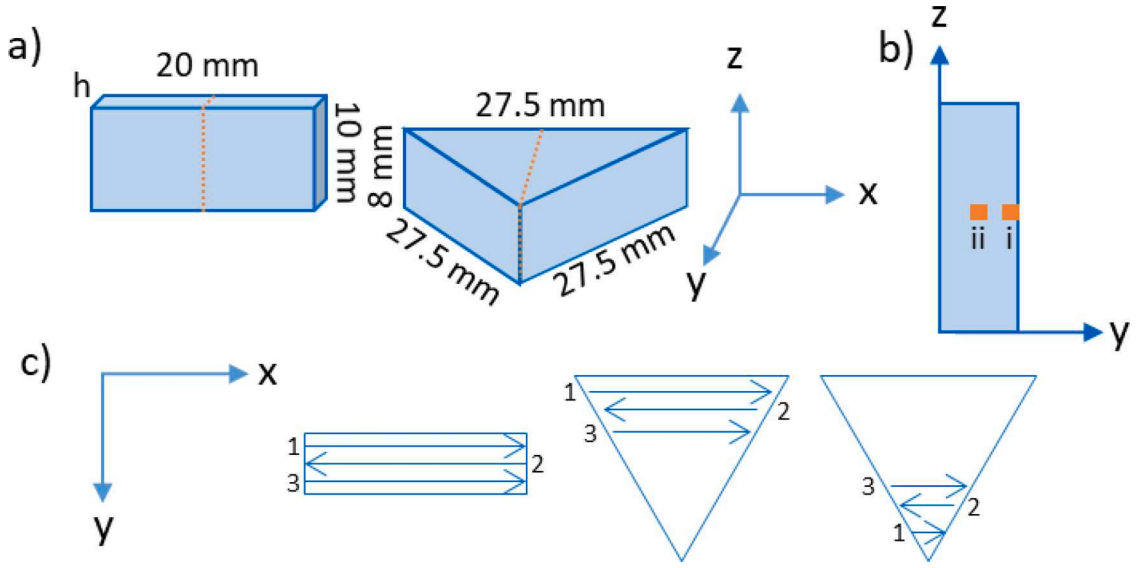

Fig. 1. Geometries of artefacts built. a) dimensions of both walls and triangular prisms along with machine axes; h is the number of hatches. orange lines show sectioning direction; b) locations of TEM lamella in 10 hatch wall from the edge (i) and centre (ii); c) view from above showing hatching strategies for 1 hatch wall, 3 hatch wall and triangular prisms. Both base to tip (left) and tip to base (right) hatching shown.

For each sample, an average calculated anisotropy factor, A_{hkl}, was calculated [32], which varies between 0 for <100> directions to 1/3 for <111> directions: $A_{hkl} = \frac{h^2k^2+k^2l^2+l^2h^2}{(h^2+k^2+l^2)^2}$ [33]. Schmid factors were computed for each scanned point (in the X direction) and the maximum Schmid factor at each point was averaged for each sample. For each pixel, a kernel average misorientation (KAM) was calculated; these can be combined to give a grain average misorientation (GAM) per grain [34]. GAM values for each grain were averaged using an area-weighted average; this was calculated for each full sample and was calculated for vertical strips (250 μm wide in Y) to allow for an analysis of GAM variation with sample width.

TEM lamella were prepared from site specific locations using a Scios (FEI) dual beam FIB/FEG-SEM. A standard *in-situ* liftout procedure was used with Pt as the deposition material. Samples were attached to 3-prong Cu omniprobe grids and electron transparent windows approximately 8 um x 8 um were milled using progressively smaller ion beam currents (1 nA, 0.5 nA and finally 0.3 nA) at 30 kV. A 5 kV final clean was used to reduce FIB surface damage to the samples. One sample was extracted from the sample edge (mid X, maximum Y, mid Z) and the other from the central region (marked i and ii respectively in Fig. 1b). TEM and STEM were performed using an FEI Tecnai Osiris operated at 200 keV with FEI Super-X EDS detectors and diffraction patterns were captured to determine the precipitates present. TEM bright field and dark field images were captured using a Gatan OneView 4k camera.

2.1. Precipitation potential model

As hypothesised by Tian et al. precipitation growth and nucleation can occur not only during solidification but also during reheating from subsequent hatches and layers [20]. To capture this effect, the time within the γ'/γ" precipitation temperature range was calculated using a Rosenthal-style moving heat source model [35]. The solution used in these calculations has been modified to use a Gaussian laser beam as a reasonable approximation to the BeAM's top hat beam [36].

$$T = T_0 + \frac{2A\alpha P}{\kappa\pi^{3/2}} \int_{-\infty}^{\infty} \frac{\exp\left[-2\frac{(\xi+vt)^2+y^2}{D_b^2+8\alpha t} - \frac{z^2}{4\alpha t}\right]}{\sqrt{\alpha t}\left(D_b^2+8\alpha t\right)} dt$$

where T, final temperature; T_0, initial temperature; A, absorptivity; P, laser power; κ, thermal conductivity; $1/2\lambda = \kappa/\rho C_p = \alpha$, thermal diffusivity; ρ, density; C_p, specific heat capacity; v, laser velocity; $\xi = x - vt$, x displacement relative to laser position; t, time and D_b, laser beam diameter (Gaussian). The parameters used for these calculations are

summarised in Table 3.

The output from the model was a steady state temperature field from which the melt pool could be extracted by drawing a contour at the solidus temperature as seen in Fig. 2. The precipitation temperature range was taken as 700-900°C in line with literature values [3,9,16], with precipitate dissolution occurring between 900°C and the solidus temperature (1916°C [38]). It is assumed that precipitation kinetics are constant in the temperature range analysed, which is supported by TTT curves by Niang et al. [3].

The light blue temperature regions in Fig. 3 show the precipitation zone, which is of interest in this analysis. The length of the zone was measured, and by knowing the laser velocity, the time spent in the precipitation zone could be calculated. The temperature profiles within the dark blue regions were such that no microstructural changes were expected to occur. The temperature of the green region was above the temperature of the precipitation region; such that transformation or dissolution may occur. These regions are called dissolution zones, as at equilibrium (assuming a homogenous composition), they are expected to have negligible γ'/ γ" content. It follows that when in the dissolution region, there is no driving force for γ' nucleation, precipitates could be dissolving to help revert the material to equilibrium. The yellow temperature regions were above the solidus temperature, and were assumed to be molten. For simplicity, the centre point of each hatch was taken to be representative of the whole hatch (marked by red dots in Fig. 3d).

P1 (Fig. 3a and b) shows the precipitation zones during solidification – directly behind the melt pool. The subsequent hatch remelted this material and then precipitation occurred in the zone marked P2; the following hatch never heated the region into the precipitation region (marked as the bottom horizontal line in Fig. 3b). As the next layer was deposited (Fig. 3c), when the laser was directly above the hatch of interest, precipitation marked by P3 occurred, so some precipitation occurred, then dissolution occurred in the zone marked D1 and finally more precipitation (again, P3). In addition, the neighbouring hatch in this layer also heated the hatch of interest, marked P4. Fig. 3d shows a diagrammatic visualisation of the yz section of a wall, with the rectangles representing each individual hatch. The laser starts in the bottom left corner, the order of hatches is shown for the first 2 layers at the bottom, with light coloured hatches occurring before the dark coloured hatches. The yz section of a melt pool (overlaid onto the hatches) shows which temperature extracted for each of the hatches.

In Fig. 3e, three hatch locations were marked with a thick border as worked examples (i, ii and iii); again, using shading to show the hatch order. Examining the precipitation in the selected location; the time spent in the precipitation zone was calculated. After depositing, the beam moves onto the following hatch, the subsequent hatches must be considered to determine which cause the material in the selected location to be raised into the precipitation zone. The selected hatch on the left hand side at height 0 mm (marked i) was remelted by the subsequent hatch (marked P2), melting any precipitates formed during solidification, but re-precipitation occurred due to P2. The subsequent layer, experienced precipitation due to P4 and then P3 as marked – by summing the time spent in these precipitation regions, the cumulative precipitation potential could be calculated.

For the hatch of interest at z=0.4 mm (ii) on the right side, there was no subsequent remelting within the same layer, so precipitation due to P1 was retained; then on the following layer, precipitation during P3 and then P4 occurred. Finally, for the hatch of interest at x=0.6 mm (iii), the P2 hatch caused remelting, so no P1 precipitation was present. In the following layer, as well as being heated by the hatch directly above it (P3), there were 2 neighbouring hatches (both P4) which contribute to the precipitation.

For each hatch, the total time in the precipitation temperature range was calculated, which effectively represents the precipitation potential of the sample. Since precipitates may dissolve/transform above 900°C, dissolution time was also calculated and subtracted from the precipitation time.

Table 3
Parameters used for Rosenthal calculations.

Parameter	Value	Reference
Step Size	5 μm	-
Thermal Conductivity, κ	9.94 $Wm^{-1}K^{-1}$	[37]
Thermal Diffusivity, α	2.87×10^{-6} m^2s^{-1}	[37]
Absorption Coefficient, A	0.45	[38]
Melting Point (solidus), T_m	1643 K	[38]
Laser Power, P	300 W	-
Laser Velocity, v	2250 mm·min^{-1}	-
Laser Beam Diameter, D_b	0.7 mm	-

3. Results

3.1. Thermal monitoring

Coaxial melt pool imagery was recorded throughout all builds and a thermal intensity for each frame calculated by summing the pixel intensities in the frame. As shown in Supplementary Fig. 1, thermal intensity values below 0.2×10^7 were at hatch ends, and hence excluded. For the base to tip triangular prism, the thermal intensities are shown in Fig. 4a and b, with an overview of the full build shown in Fig. 4b (smoothing applied), the thermal intensity can be seen to increase over the first 6-7 layers and then a plateau being reached, but with significant variation within a layer. Fig. 4b shows the thermal intensity for a layer in the plateau without any smoothing. Each hatch can be seen as the thermal intensity drops to 0 between hatches and the hatch length can be seen to decrease as the tip is approached, with the thermal intensity increasing closer to the tip.

Similar plots are shown for the 6 hatch wall in Fig. 4c and d, again with the overall intensity shown to increase with build time, but in this case, more layers were required before the plateau was reached, potentially due to the shorter layers. Fig. 4d shows the thermal intensity of 2 layers, exhibiting a clear trend with the central hatches having higher thermal intensity than edge hatches.

The average intensity for each wall (excluding points below 0.2×10^7) is shown in Fig. 4e. The thermal intensity increases with hatch number up to 3 hatches, from there, the thermal intensity drops until a plateau at a thickness of 8 hatches.

3.1.1. Hardness Analysis

Hardness maps were taken from two sections of the triangular prisms as shown in Fig. 5a and b. The slanted and bottom edges of the xy section were observed to be softer than the bulk (Fig. 5a) and Fig. 5c shows that the edges (along the y axis) are softer than the bulk. A longer drop-off is seen at large y values, which is where the tip of the triangular prism is.

The hardness distribution in the walls is summarised in Fig. 6. Fig. 6a shows the hardness variation in the y axis. For most walls, the peak hardness is at the centre, with notable hardness drop-offs within 1 mm of the edges. For this reason, the peak hardness increases with wall thickness until the 6 hatch wall after which there is minimal change. Fig. 6b shows the average hardness for each wall with respect to sample thickness. Again, the average hardness increases with sample thickness until 2-3 mm at which point the hardness plateaus. Table 4 shows the average hardness for each section of each sample. The bottom row of indents (in z) was disregarded, due to the heat-sink effect of the substrate. For each section, a single indent along each external edge of the sample was removed; these are referred to as edge hardness' and the remaining indents were classed as centre hardness' as summarised in Table 4. Unpaired 2 sample t-tests (α=0.05) were performed for each sample between the centre and the edge and the results are shown in Table 4.

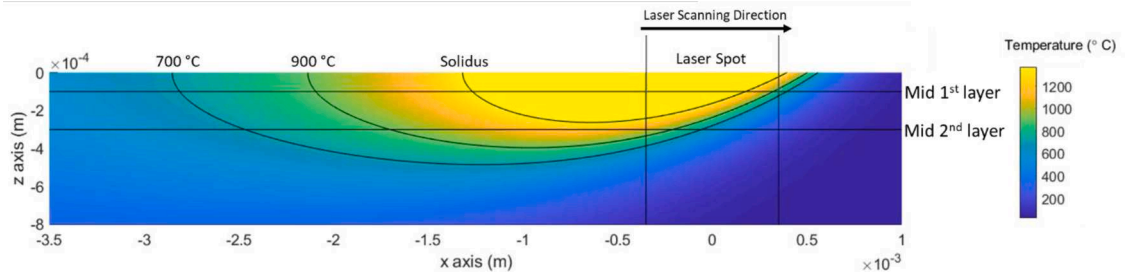

Fig. 2. Temperature field output from moving laser source model; side on (XZ) view showing the laser position and contours at the solidus temperature, 700°C and 900°C. Horizontal lines shown halfway through subsequent layers.

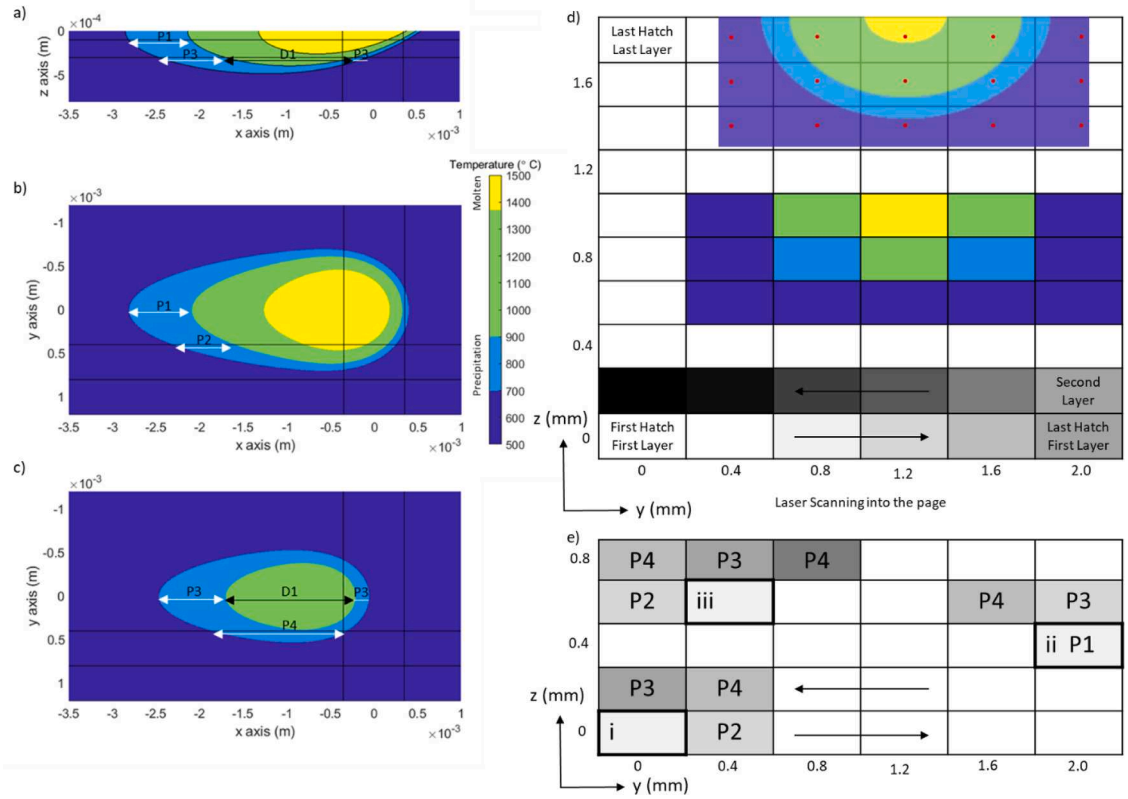

Fig. 3. Diagram showing the calculations for precipitation potential during DED. a) xz section at maximum length of melt pool, as in Fig. 2, colour scale set to show different key regions during cooling. b) xy section at mid-1st layer (as marked in Fig. 2), precipitation regions shown for the current hatch (P1) and the subsequent hatch (P2). c) xy section at mid-2nd layer (as marked in Fig. 2), precipitation regions shown for the next layer (P3) and the subsequent hatch in the next layer (P4). d) yz cross section of a 6 hatch wall, laser scans into the page, hatching order shown by arrows, alternating each layer; shading shows the hatch order in the first 2 layers from light (first hatch) to dark (later hatch). Also shown is a yz section of the melt pool with the red dots showing the centre points at which analysis was undertaken. e) 3 examples of precipitation shown on the same layout as in d. These are marked i, ii and iii and for each, the subsequent hatches are shaded, becoming darker with time.

3.1. EBSD

EBSD maps of the yz sections of the walls were used to understand the grain structure. Maps were constructed through the full thickness (y) and a height of at least 1.5 mm (z) (Fig. 7). The results indicated that the single hatch was symmetrical, with grains growing from the edges downwards towards the centre and a variety of orientations present. Samples with 2 and 3 hatches were progressively more oriented along <100> with more grains aligned in the growth direction and some large grains in the 3 hatch sample. Samples consisting of 4, 6 and 8 hatches were all predominantly of <111> orientation (blue/purple) with long grains growing along the height of the walls.

Small equiaxed grains with no dominant orientation were found to form where the laser had passed. Between these centres, there are grains which propagate through many layers, forming large elongated grains. The average hardness values are plotted against the anisotropy factor [33] for the 6 walls in Fig. 7i. No clear trends are visible, with 1-3 hatch walls decreasing in hardness with increasing anisotropy factor, whereas wider walls show little variation in either hardness or anisotropy factor. Fig. 7h shows the distribution of GAM for each grain in the 6 hatch wall; the large grains appear to have the highest GAM values. There seems to be no clear trend in GAM between the edges and the centre of the sample.

3.2. Precipitate Analysis

TEM was performed on one edge sample and on one central sample, no precipitates were visible in any samples using bright field imaging.

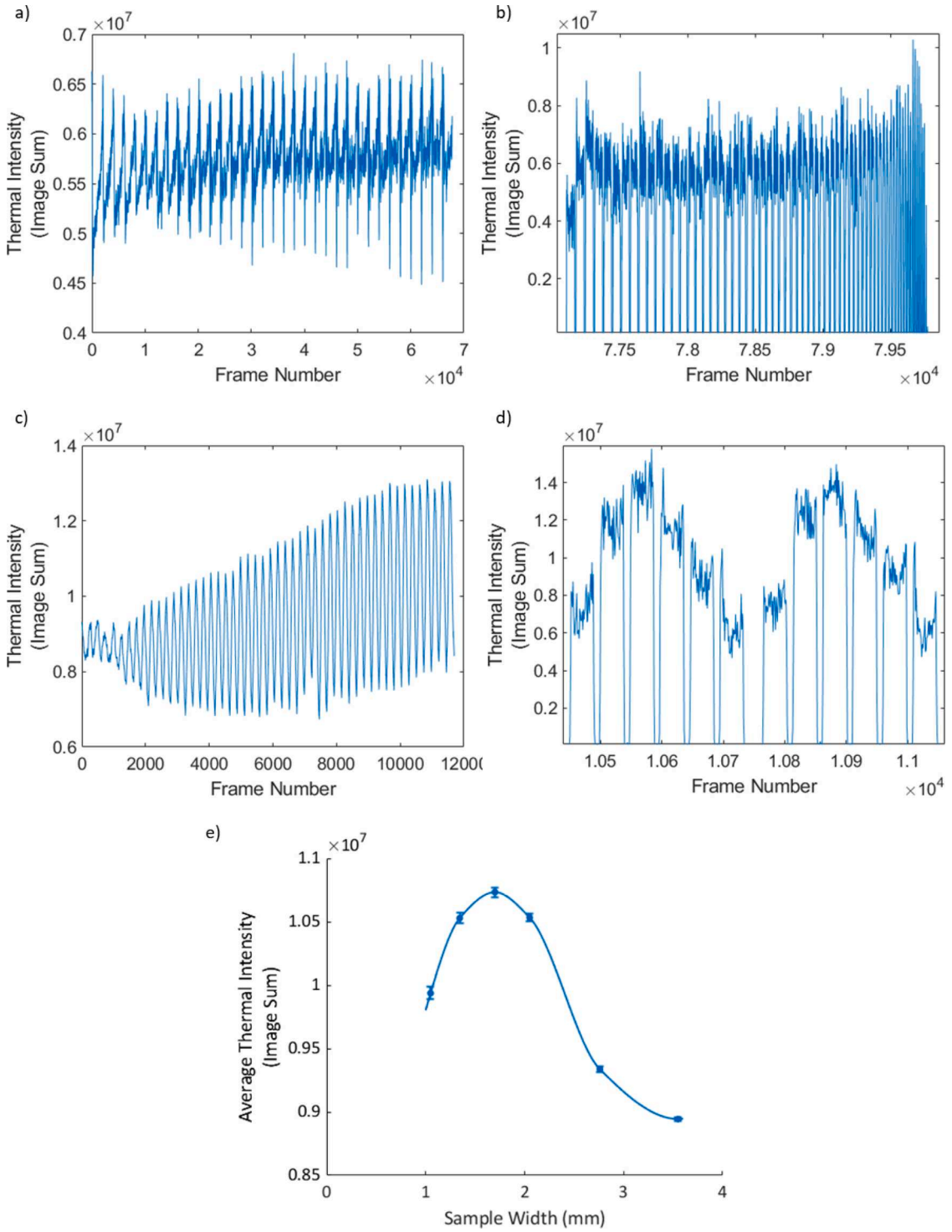

Fig. 4. a, b) thermal data from base to tip triangular prism showing the thermal intensity with frame number a) full build, values below 0.2×10^7 removed and a moving mean of width 100 points applied b) single layer without any data filtering/smoothing; c, d) thermal data of 6 hatch wall showing the thermal intensity with frame number, c) full build, values below 0.2×10^7 removed and a moving mean of width 100 points applied d) two layers without any data filtering/smoothing; e) average thermal intensity ($<0.2 \times 10^7$ removed) for each wall, error bars showing standard error.

However, the central sample showed diffraction patterns representative of γ' precipitates, which were not visible in the edge sample (as seen in Fig. 8c and a respectively).

3.2.1. *Precipitation Potential*

The total times in the precipitation region are plotted in Fig. 9a for walls of 1-4 hatches, with colouring showing longer precipitation times in grey and shorter times in blue. It can be clearly seen that the top surface experiences the least time in the precipitation zone, followed by the outside walls. The bulk of the samples experiences the longest time in the precipitation zone, which is estimated to be ~0.095 s.

Since dissolution rates are not accurately known, the same calculations were repeated, but without subtracting dissolution times (i.e. sum of precipitation times only). This is shown in Fig. 9b with similar trends

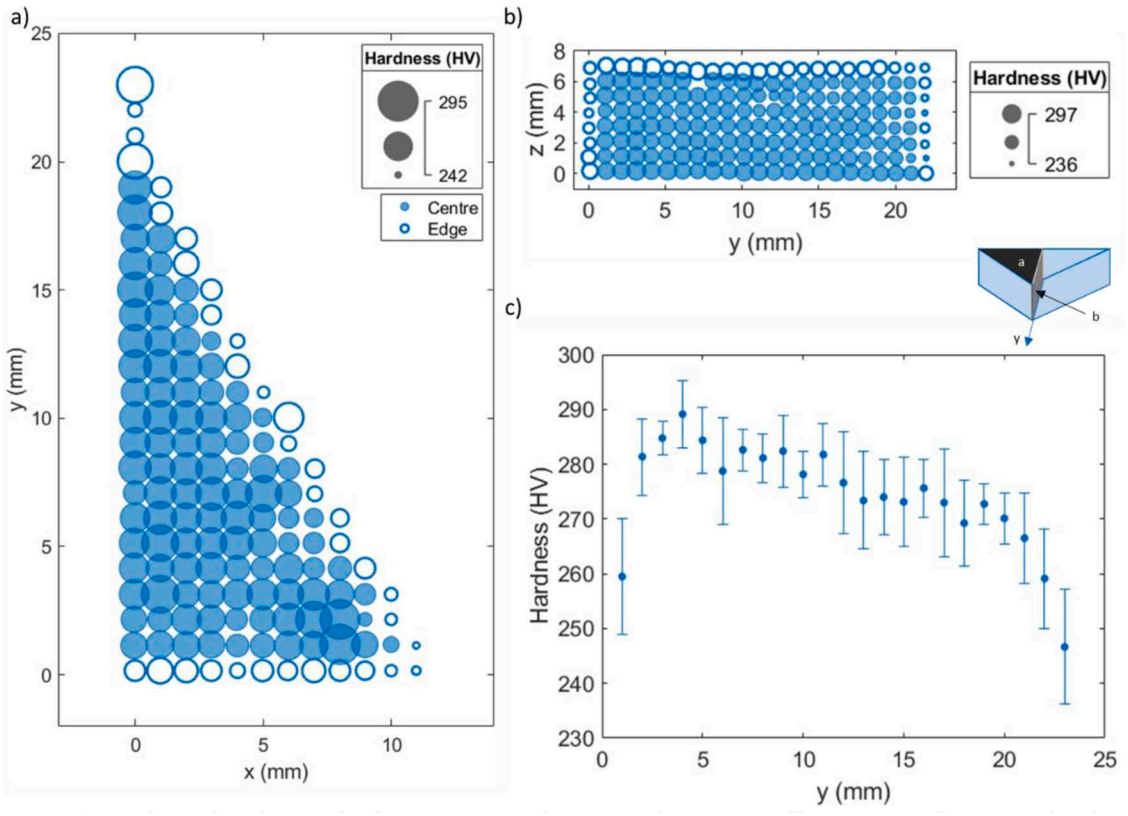

Fig. 5. Hardness distribution for base-tip triangular prism a) xy section b) yz section c) average hardness along y direction as calculated from yz section, standard deviation shown. Inset shows cross-sections taken and positive y direction.

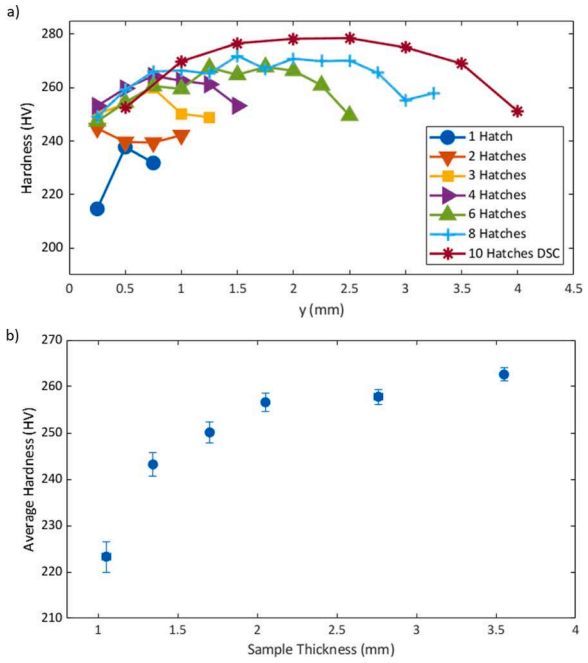

Fig. 6. Hardness plots of walls a) with thickness (y axis), showing maximum hardness at centre of the wall b) average hardness of walls plotted against sample thickness, standard error shown (thickness errors hidden by data point due to small magnitude).

but an increased maximum duration of 0.14 s.

4. Discussion

The hardness maps of triangular prisms (Fig. 5a) show that the external edges are softer than the centre. The same pattern can be seen in the walls, with maximum hardness at the wall centres (Fig. 6a). It could be expected that this would be derived from the melt pool morphology. Fig. 4d shows the thermal intensity, which has been shown to be representative of the melt pool size (Supplementary Fig. 1). The same pattern can be seen, with the edges having a lower thermal intensity corresponding to the lower hardness.

However, when looking at the average thermal intensities for the walls, the maximum intensity is for the 3 hatch wall, with dropping intensity either side (Fig. 4e). The average hardness values for walls increases with thickness until a plateau is reached following 4 hatches. Since the overall hardness of the walls doesn't correlate with the thermal intensities, it can be concluded that the measured hardness values are not directly derived from the melt pool morphology.

A decrease of hardness with height has previously been reported in Inconel 718 [20] and Fig. 6a shows a hardness variation with sample width within a component. To quantify the hardness differences between the edges and the centres of samples, the hardness indents were classified as follows:

- Indents in the bottom row (z, closest to substrate) were removed
- Indents in the top row and nearest indent to any other external face were classified as edge indents
- The rest of the indents were classified as centre indents.

Two sample t-tests show that for both triangular prisms, there is a statistically significant ($p<0.05$) decrease in hardness in the edge indents (Table 4). The decrease in the yz section of the tip to base

Table 4
Table summarising average hardness values for all walls and triangular prisms. Showing centre and edge value separately to test whether these are significantly different (two sample t-tests were used to determine statistical significance using $p<0.05$).

	Sample	No. Indents	Average Hardness - HV (Standard Error) Full Sample	Edges	Centre	Statistically significant difference between centre and edge hardness
	1 hatch wall	36	223.3 (3.3)	218.9 (3.8)	233.6 (5.2)	Yes
	2 hatch wall	52	243.2 (2.6)	240.1 (3.7)	239.9 (2.9)	No
	3 hatch wall	68	250.1 (2.2)	245.4 (3.7)	253.6 (2.0)	Yes
	4 hatch wall	84	256.6 (2.0)	249.1 (3.6)	261.2 (1.5)	Yes
	6 hatch wall	136	257.8 (1.6)	246.7 (3.5)	261.6 (0.8)	Yes
	8 hatch wall	176	262.6 (1.4)	252.9 (3.4)	265.2 (0.5)	Yes
	10_DSC wall	128	267.8 (1.7)	253.2 (3.4)	274.0 (0.5)	Yes
Base to Tip Triangular Prism	YZ section (rectangular)	184	273.4 (0.9)	264.3 (2.7)	276.0 (0.8)	Yes
	XY section (triangular)	142	264.6 (0.9)	254.3 (1.6)	267.9 (0.9)	Yes
	Combined	326	272.7 (0.7)	259.3 (1.6)	272.3 (0.6)	Yes
Tip to Base Triangular Prism	YZ section (rectangular)	184	275.6 (0.9)	274.0 (2.9)	276.1 (0.9)	No
	XY section (triangular)	155	260.8 (0.9)	251.3 (1.3)	263.5 (0.9)	Yes
	Combined	339	268.3 (0.7)	262.3 (2.1)	269.9 (0.7)	Yes

triangular prism was not statistically significant, but when combined with the xy section, then the whole part was significantly harder in the centre. Walls were built with different numbers of hatches to simplify the geometry and identify the source of the hardness variation.

For 6 of the 7 walls, the centre was statistically significantly harder than the edges (Table 4). For a 1 hatch wall, this model does not predict lateral variation as there are not multiple hatches in a layer, however, hardness variation is measured (Fig. 6a); this can likely be explained by the change in heat transfer mechanisms at component edges, convection and radiation become more significant (Rosenthal model only considers conduction), reducing the time spent in the precipitation region. The largest changes in average hardness were found in walls from 1- 3 hatches wide (Fig. 6b), with slight further increases with wall width. This continued increase is not captured in the precipitation model (Fig. 9), this could be as a result of the different heat-flow effects aforementioned or the second lateral hatch could also be having an effect (which is not predicted by the Rosenthal model, but this could be due to the modelling of a Gaussian heat source, rather than the top hat source used experimentally). The main changes in hardness from 1 -3 hatches are captured by the precipitation potential model.

EBSD maps of the walls were analysed (Fig. 7) and show differences in preferential orientation between the walls. In the 3 thicker walls, the predominant texture is near the <111> direction (purple on IPF map). For the narrower walls, there is more significant variation, but with a noticeable tendency towards the <100> direction (red). The anisotropy factor, A_{hkl}, is a simple way of condensing the orientations into a single number, with <100> being 0, <110> being 0.25 and <111> being 0.33. Since literature reports that Young's modulus should increase in the same manner, $E_{<100>} < E_{<110>} < E_{<111>}$ [39], and hardness being proportional to Young's modulus [40,41], it would be expected that hardness would correlate with the average anisotropy factor. This is not the case as shown in Fig. 7i, thus the hardness cannot be directly explained by the crystallographic structure [5].

Due to the Hall-Petch effect, a finer grain size would be expected to lead to a higher hardness, this is the opposite trend to that shown in Fig. 7i, as discussed in Supplementary Section 5.2. There is variation in hardness with width (Fig. 6a), however, the hardness indent spacing was purposefully offset from the hatch spacing, so the regular patterns in grain size (Fig. 7) cannot be used to explain the trend in hardness. The large grains, however, have a higher average GAM (Fig. 7h), and thus a higher dislocation density. This partially explains the variation in GAM with width, however, there is no consistent decrease in GAM at component edges, so this cannot be concluded to be the dominant mechanism behind the hardness trends observed. There is a monotonic increase in GAM with sample width (Supplementary Fig. 2), similar to hardness (Fig. 6a), suggestive of some underlying effect of dislocation density on the component hardness.

None of the electron diffraction patterns obtained from all samples show reflections representative of γ" precipitates, suggesting their absence. The foil from the centre of the sample did show superlattice reflections in the selected area diffraction pattern corresponding to the γ' phase (Fig. 8c). The dark field image from a superlattice reflection is shown in Fig. 8d. Intensity corresponding to a large number of fine γ' particles can be observed, however the resolution was insufficient to probe the morphology of individual particles in any great detail. STEM imaging (Fig. 8b) showed insufficient contrast between phases to clearly observe the γ' particles. These results indicate that the centre of the as-built samples suggest the presence of extremely fine γ' precipitates (likely less than 5 nm), whilst in the sample edges there were no γ' superlattice reflections visible, suggesting their absence. DSC suggests a larger sinusoid in the γ' region for the centre of the sample than for the tip sample consistent with these observations, as discussed in Supplementary Section 5.4.

TEM data suggests that the hardness differences could be due to a change in γ' precipitate fraction. Hardness in the yz section of the triangular prism (Fig. 5c) varies between 247-289 HV, leading to a ~40HV variation. When taking walls into consideration similar peak hardness values of 290-300 HV were seen, but with hardness values as low as 215 HV recorded (Fig. 6a). This overall range of ~80 HV originates from averaged values, and thus has not been skewed by outlier values. Tian *et al.* concluded that in their as-built DED samples, the hardness variation was due to γ" precipitation; however, TEM has not

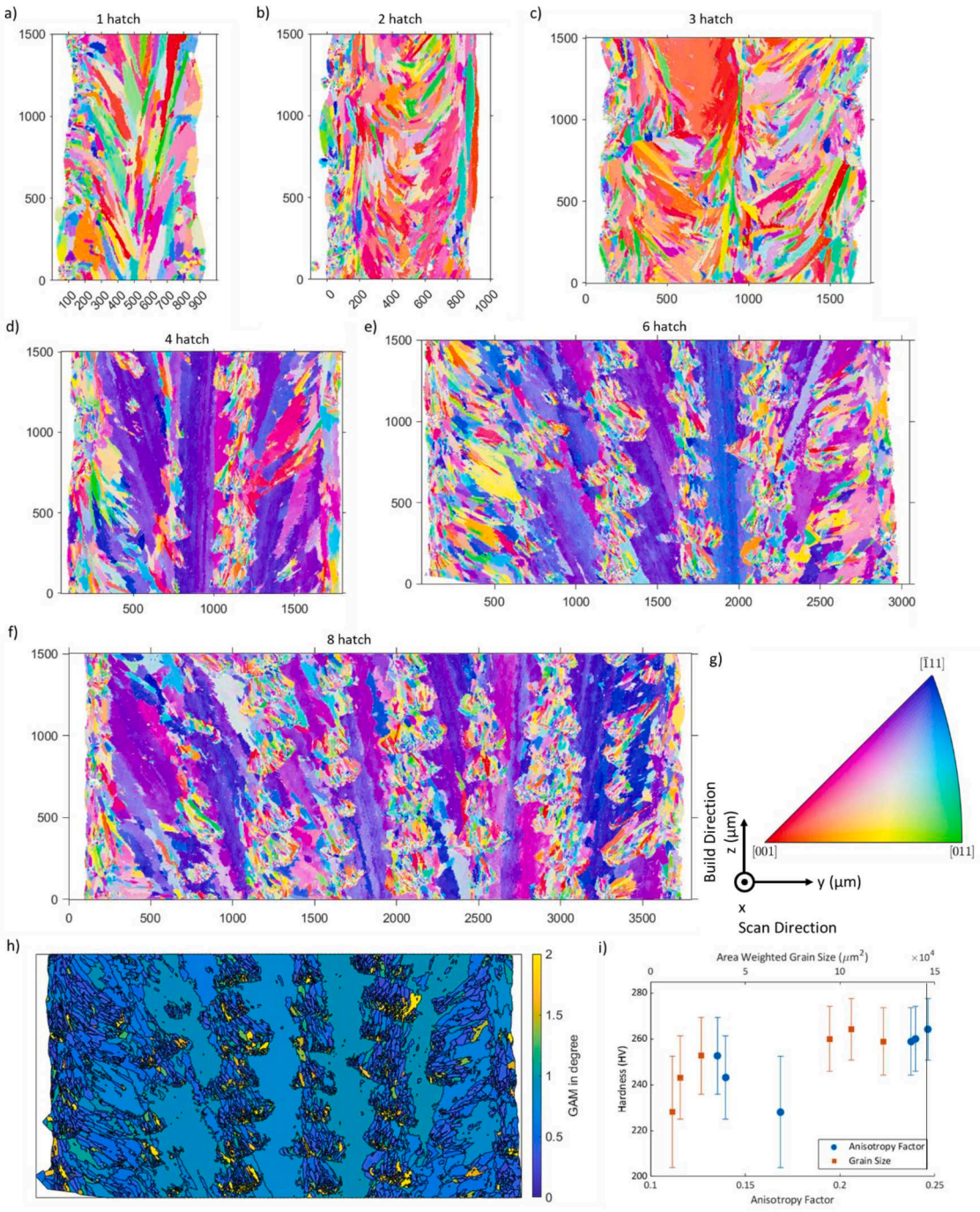

Fig. 7. a-f) Inverse pole Fig. (IPFX) maps of YZ section of walls from 1 - 8 hatches showing full thickness (Y) and 1500 μm height (Z) at the midpoint of the height, g) axis definitions and key for IPF maps; h) grain average misorientation (GAM) of the 6 hatch wall included; i) plot of hardness against anisotropy factor and weighted grain size for the 6 walls of varying thicknesses shown on bottom axis. Standard deviations of hardness shown.

shown any evidence indicating the presence of these precipitates in this study.

A Rosenthal-based moving heat source model [35] was used to calculate the time spent in the precipitation temperature range (700-900°C) for the walls. These models, albeit not numerically accurate, give a realistic temperature distribution around the melt pool in bulk material. For this reason, they are referred to as a precipitation potential rather than attempting to estimate precipitate volume fractions. Time spent above 900°C but below the solidus promotes either transformation to the δ phase, or dissolution of the γ'/γ" precipitates. Assuming this dissolution rate is equal to the precipitation rate, the time in this temperature range can be simply subtracted from the time in the precipitation zone (Fig. 9a). The top surface spends up to 4.5x less time in the precipitation zone than the bulk, which would explain the lower hardness, with the external edges spending 2x less.

However, there are reports of samples being heated to 1100°C and cooled at 10°C/min, so spending 21 mins in the dissolution range, yet still with large amounts of γ" retained [3]; increased time at temperature is likely to encourage transformation from γ' to γ". For this reason, it was decided that the dissolution of precipitates would be ignored, and calculations would only consider the time in the precipitation temperature range (Fig. 9b). An identical trend was observed, but with a larger variation between centre and edge (up to 6.7x). The maximum precipitation time was 0.14 s, above the 0.1 s "nose" of the TTT curve [3]. The

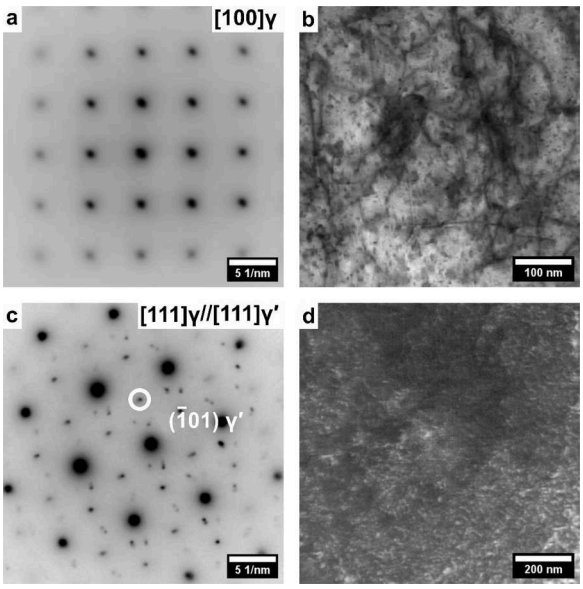

Fig. 8. TEM diffraction patterns from 10 hatch wall a) SADP of matrix from edge of samples (equiaxed grain), showing FCC γ pattern; b) TEM bright field of the γ matrix; c) SADP of matrix from centre of samples (columnar grain); d) corresponding dark field image taken using the circled superlattice reflection in c.

times are of the correct order to experience precipitation and the variation is in the expected positions with edges and top surfaces having shorter times and thus less precipitation that leads to a softer material. As shown by Kumara *et al.* [18], γ" precipitation in the interdendritic regions can be an order of magnitude quicker than at the dendrite core due to local segregation. It logically follows that the same could be expected for γ' precipitation, segregation due to solidification will increase the solute content and further promote precipitation. It is feasible that 0.01 s in the temperature range 700-900°C could be sufficient for precipitation to initiate.

The maximum precipitation potential increases from 1 hatch to 3 hatches, which would explain the increase in centre hardness with thickness as observed in Fig. 6b. The precipitation range used was 700-900°C, but there is sub-second precipitation down to ~650°C. The precipitation at this temperature would be slower, but would still increase the time in the precipitation zone. The Rosenthal model estimated the movement of a single laser hatch, but it is known that during the build, the component retains heat. This would increase the temperature of the component and likely increase the melt pool size, but also increase the duration in the precipitation zone. Since these effects increase the precipitation potential in all parts of the sample, they would not be expected to change the key trends. This analysis focusses on the central point of each hatch, this snapshot will not be numerically accurate for the whole sample e.g. slightly above the centre, the melt pool and precipitation regions will be larger and slightly below, they will be smaller. The centre points should be representative of the bulk and any error would be systematic, hence this would not affect the results of the model.

This works confirms the hypothesis that γ' precipitates are the first to form [12–15] as TEM suggests presence of γ' precipitates, but no sign of γ" precipitates. Given that Inconel 718 is predominantly thought of as a γ" strengthened alloy, it is important to acknowledge that in the as-built state, the components are actually γ' strengthened. It is likely that when heat treated, γ" would precipitate and this would take over as the primary strengthening phase. The precipitation potential model predicts the component edges to be lacking in precipitates, explaining the reduced hardness measured.

It has been shown that these effects occur within a layer as well as with build height, causing hardness variation on the component scale. When printing complex geometries, both wide and narrow sections would be expected. The walls show a 35 HV hardness difference between a 1 mm and a 3.5 mm section with the tip of the triangular prism being 40 HV softer than the centre. Since the tip is narrower, the hatches are shorter and so the time at temperature will be decreased. This explains why there is a drop-off in hardness in the last 3 mm of the triangular prism (Fig. 5c).

Fig. 6a shows that in any component, a region of ~1 mm around the edges is softer than the centre. This is critical as when components are being repaired, consistent properties are required. In addition, any components narrower than 2-3 mm never reach peak hardness. These factors affect the design process for printing complex shapes in DED. For consistent mechanical properties, sections should be designed to be wider than 3mm, with 1mm on the edges removed post process; alternatively, the design must account for the fact that sections thinner than 3mm will have dissimilar properties.

Alternatively, the idea of precipitation kinetics could be used to create a build strategy which would result in a homogeneous component. For example, if the edge of the sample is in the precipitation zone for 0.5 s, compared to 1.4 s in the centre, then theoretically, the edge needs a subsequent 0.9 s precipitation for a constant hardness. Using the Rosenthal based model, an in-situ heat treatment (reheating the sample

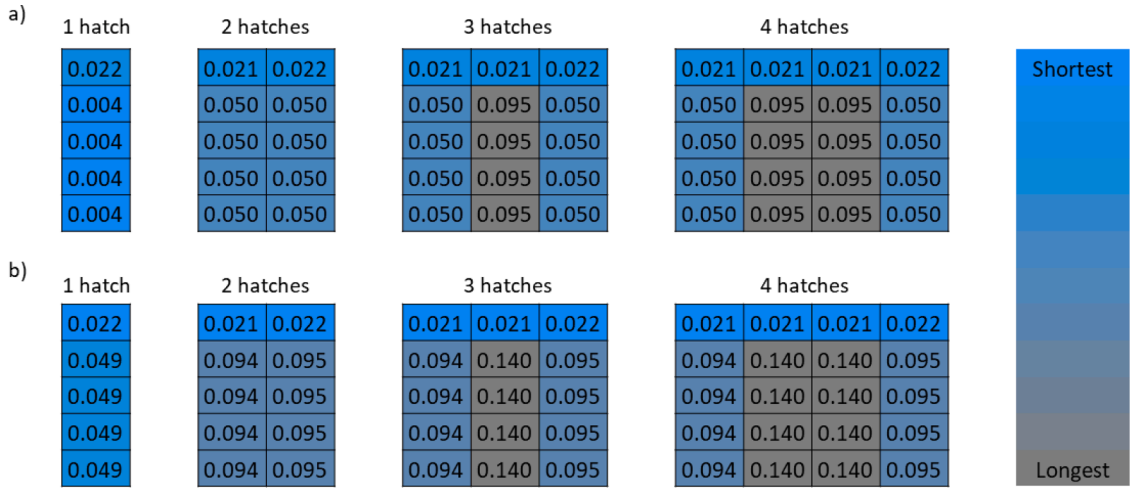

Fig. 9. Precipitation times (s) output from the precipitation potential model, showing yz section. For walls wider than 4 hatches, the same edge pattern remains. a) sum of time in precipitation regions, subtracting time in dissolution zone. b) sum of time in precipitation regions, assuming dissolution is negligible.

without melting it) could be calculated and applied. This is similar to the application of in-situ heat treatment to EB-PBF by Sames et al [4]. The same technique could be used to increase the hardness of a thin sample by rescanning it and so creating an as-built thin sample with the higher hardness experienced in a wider sample.

Since the thermal intensity is related to the melt pool area, the melt pool dimensions of the Rosenthal model can be adapted depending on the current melt pool monitoring. It would be possible to create a variety of melt pools in the Rosenthal model and select appropriate ones depending on the current thermal intensity. This way, a live calculation of precipitation time could be made and an adaptive in-situ heat treatment could be implemented automatically. This would allow for building of complex shaped right-first-time components with constant hardness in DED.

5. Conclusion

It has been shown that in as-built Inconel 718, there are significant hardness variations in both the build plane and the build direction. Despite Inconel 718 being a γ" strengthened alloy, evidence for the presence of γ' has been found (with no γ" present) and the increased precipitation/growth of γ' precipitates caused by the material being in the precipitation temperature range for longer can be related to the increased hardness. Common factors such as melt pool morphology and crystallographic structure have been shown not to be the driving factor behind the hardness variation.

A precipitation kinetic model based on a simple moving heat source model has been created to calculate the time different sections of the component spent in the precipitation temperature range. The time spent in the precipitation temperature range is shown to correlate with the hardness, confirming that the increase in hardness is caused by γ' precipitation, with strengthening calculations corroborating this. This could be used to calculate in-situ heat treatments, which would result in consistent hardness in complex components. Further, using the coaxial monitoring, an in-situ control algorithm could be used to homogenise each component directly after being built.

Data availability

Data supporting this publication can be freely downloaded from 10.5281/zenodo.6451775 under the terms of the Creative Commons Attribution (CC BY) licence.

Declaration of interests

The authors declare that they have no known competing financial interests or personal relationships that could have appeared to influence the work reported in this paper.

The authors declare the following financial interests/personal relationships which may be considered as potential competing interests:

CRediT authorship contribution statement

Lova Chechik: Conceptualization, Methodology, Investigation, Software, Writing – original draft. **Katerina A. Christofidou:** Conceptualization, Writing – review & editing. **Jonathon F.S. Markanday:** Investigation, Conceptualization, Writing – review & editing. **Alexander D. Goodall:** Writing – review & editing, Visualization. **James R. Miller:** Investigation, Formal analysis, Writing – review & editing. **Geoff West:** Resources, Investigation. **Howard Stone:** Resources, Funding acquisition. **Iain Todd:** Conceptualization, Writing – review & editing, Supervision, Funding acquisition.

Declaration of Competing Interest

The authors declare that they have no known competing financial interests or personal relationships that could have appeared to influence the work reported in this paper.

Acknowledgments

This work was supported by the EPSRC Rolls-Royce Strategic Partnership Grant, MAPP (grant EP/P006566/1) and EPSRC (grant EP/R512175/1). The provision of materials and supporting information from Rolls-Royce plc. is gratefully acknowledged. We also wish to acknowledge the Henry Royce Institute for Advanced Materials, funded through EPSRC grants EP/R00661X/1, EP/S019367/1, EP/P02470X/1 and EP/P025285/1, for BeAM Magic 2.0 access at The University of Sheffield and also for FEG JSM-7900F SEM access at Royce@Sheffield. Thanks to Dr. Le Ma for operation of the SEM and to Dr Oday Hussain for operation of the DSC. For the purpose of open access, the author has applied a Creative Commons Attribution (CC BY) licence to any Author Accepted Manuscript version arising.

Supplementary materials

Supplementary material associated with this article can be found, in the online version, at doi:10.1016/j.mtla.2022.101643.

References

[1] C. Slama, M. Abdellaoui, Structural characterization of the aged Inconel 718, J. Alloys Compd. 306 (2000) 277–284, https://doi.org/10.1016/S0925-8388(00)00789-1.
[2] M.M. Attallah, R. Jennings, X. Wang, L.N. Carter, Additive manufacturing of Ni-based superalloys: The outstanding issues, MRS Bull 41 (2016) 758–764, https://doi.org/10.1557/mrs.2016.211.
[3] A. Niang, B. Viguier, J. Lacaze, Some features of anisothermal solid-state transformations in alloy 718, Mater. Charact. 61 (2010) 525–534, https://doi.org/10.1016/j.matchar.2010.02.011.
[4] W.J. Sames, K.A. Unocic, G.W. Helmreich, M.M. Kirka, F. Medina, R.R. Dehoff, S. S. Babu, Feasibility of in situ controlled heat treatment (ISHT) of Inconel 718 during electron beam melting additive manufacturing, Addit. Manuf. 13 (2017) 156–165, https://doi.org/10.1016/j.addma.2016.09.001.
[5] Y.C. Yeoh, G. Macchi, E. Jain, B. Gaskey, S. Raman, G. Tay, D. Verdi, A. Patran, A. M. Grande, M. Seita, Multiscale microstructural heterogeneity and mechanical property scatter in Inconel 718 produced by directed energy deposition, J. Alloys Compd. 887 (2021), 161426, https://doi.org/10.1016/j.jallcom.2021.161426.
[6] A. Devaux, L. Nazé, R. Molins, A. Pineau, A. Organista, J.Y. Guédou, J.F. Uginet, P. Héritier, Gamma double prime precipitation kinetic in Alloy 718, Mater. Sci. Eng. A. 486 (2008) 117–122, https://doi.org/10.1016/j.msea.2007.08.046.
[7] J. Scott, N. Gupta, C. Weber, S. Newsome, Additive manufacturing: Status and opportunities, Sci. Technol. Policy Inst. (2012) 1–19. https://cgsr.llnl.gov/content/assets/docs/IDA_AdditiveM3D_33012_Final.pdf.
[8] B. Blakey-Milner, P. Gradl, G. Snedden, M. Brooks, J. Pitot, E. Lopez, M. Leary, F. Berto, Metal additive manufacturing in aerospace : A review, Mater. Des. 209 (2021), 110008, https://doi.org/10.1016/j.matdes.2021.110008.
[9] S.L. Semiatin, N.C. Levkulich, R. Larsen, J.S. Tiley, K.N. Wertz, F. Zhang, T. M. Smith, R.Y. Zhang, H.B. Dong, P. Gadaud, J. Cormier, The Application of Differential Scanning Calorimetry to Investigate Precipitation Behavior in Nickel-Base Superalloys Under Continuous Cooling and Heating Conditions, Metall. Mater. Trans. A Phys. Metall. Mater. Sci. 52 (2021) 3706–3726, https://doi.org/10.1007/s11661-021-06362-x.
[10] P. Kürnsteiner, M.B. Wilms, A. Weisheit, B. Gault, E.A. Jägle, D. Raabe, High-strength Damascus steel by additive manufacturing, Nature 582 (2020), https://doi.org/10.1038/s41586-020-2409-3.
[11] T.M. Smith, N.M. Senanayake, C.K. Sudbrack, P. Bonacuse, R.B. Rogers, P. Chao, J. Carter, Characterization of nanoscale precipitates in superalloy 718 using high resolution SEM imaging, Mater. Charact. 148 (2019) 178–187, https://doi.org/10.1016/j.matchar.2018.12.018.
[12] A. Balan, M. Perez, T. Chaise, S. Cazottes, D. Bardel, F. Corpace, F. Pichot, A. Deschamps, F. De Geuser, D. Nelias, Precipitation of γ″ in Inconel 718 alloy from microstructure to mechanical properties, Materialia 20 (2021), 101187, https://doi.org/10.1016/j.mtla.2021.101187.
[13] C. Kumara, A. Segerstark, F. Hanning, N. Dixit, S. Joshi, J. Moverare, P. Nylén, Microstructure modelling of laser metal powder directed energy deposition of alloy 718, Addit. Manuf. 25 (2019) 357–364, https://doi.org/10.1016/j.addma.2018.11.024.
[14] R. Cozar, A. Pineau, Morphology of γ' and γ'' precipitates and thermal stability of Inconel 718 type alloys, Metall. Mater. Trans. B. 4 (1973) 47–59, https://doi.org/10.1007/BF02649604.
[15] A.J. Detor, R. Didomizio, R. Sharghi-moshtaghin, N. Zhou, R. Shi, Y. Wang, D.P. Mcallister, M.J. Mills, Enabling Large Superalloy Parts Using Compact

Coprecipitation of γ' and γ'', Metall. Mater. Trans. A. 49 (n.d.) 708–717. https://doi.org/10.1007/s11661-017-4356-7.
[16] B. Saleem, H. Dong, Phase Characterization of CRA Fastener INCONEL718 in Relation of Hydrogen Assisted Cracking, Mater, Today Proc. 2 (2015) S383–S392, https://doi.org/10.1016/j.matpr.2015.05.053.
[17] J.H. Boswell, D. Clark, W. Li, M.M. Attallah, Cracking during thermal post-processing of laser powder bed fabricated CM247LC Ni-superalloy, Mater. Des. 174 (2019), 107793, https://doi.org/10.1016/j.matdes.2019.107793.
[18] C. Kumara, D. Deng, F. Hanning, M. Raanes, J. Moverare, P. Nylén, Predicting the Microstructural Evolution of Electron Beam Melting of Alloy 718 with Phase-Field Modeling, Metall. Mater. Trans. A Phys. Metall. Mater. Sci. 50 (2019) 2527–2537, https://doi.org/10.1007/s11661-019-05163-7.
[19] H.L. Wei, T. Mukherjee, W. Zhang, J.S. Zuback, G.L. Knapp, A. De, T. DebRoy, Mechanistic models for additive manufacturing of metallic components, Prog. Mater. Sci. (2021) 116, https://doi.org/10.1016/j.pmatsci.2020.100703.
[20] Y. Tian, D. McAllister, H. Colijn, M. Mills, D. Farson, M. Nordin, S. Babu, Rationalization of microstructure heterogeneity in Inconel 718 builds made by the direct laser additive manufacturing process, Metall. Mater. Trans. A Phys. Metall. Mater. Sci. 45 (2014) 4470–4483, https://doi.org/10.1007/s11661-014-2370-6.
[21] T. DebRoy, H.L. Wei, J.S. Zuback, T. Mukherjee, J.W. Elmer, J.O. Milewski, A. M. Beese, A. Wilson-Heid, A. De, W. Zhang, Additive manufacturing of metallic components – Process, structure and properties, Prog. Mater. Sci. 92 (2018) 112–224, https://doi.org/10.1016/j.pmatsci.2017.10.001.
[22] W.J. Sames, K.A. Unocic, R.R. Dehoff, T. Lolla, S.S. Babu, Thermal effects on microstructural heterogeneity of Inconel 718 materials fabricated by electron beam melting, J. Mater. Res. 29 (2014) 1920–1930, https://doi.org/10.1557/jmr.2014.140.
[23] S. Zhang, X. Lin, L. Wang, X. Yu, Y. Hu, H. Yang, L. Lei, W. Huang, Strengthening mechanisms in selective laser-melted Inconel 718 superalloy, Mater. Sci. Eng. A. 812 (2021), 141145, https://doi.org/10.1016/j.msea.2021.141145.
[24] J.E. Bailey, P.B. Hirsch, The dislocation distribution flow stress and stored energy in cold worked crystalline silver, Philos. Mag. 5 (1960), https://doi.org/10.1080/14786436008238300.
[25] M. Calcagnotto, D. Ponge, E. Demir, D. Raabe, Orientation gradients and geometrically necessary dislocations in ultrafine grained dual-phase steels studied by 2D and 3D EBSD, Mater. Sci. Eng. A. 527 (2010) 2738–2746, https://doi.org/10.1016/j.msea.2010.01.004.
[26] Z. Zribi, H.H. Ktari, F. Herbst, V. Optasanu, N. Njah, XRD and EBSD, SRS characterization of a casting Al-7wt%Si alloy processed by equal channel angular extrusion: Dislocation density evaluation, Mater. Charact. 153 (2019) 190–198, https://doi.org/10.1016/j.matchar.2019.04.044.
[27] I. Carneiro, S. Simoes, Recent Advances in EBSD Characterization of Metals, Metals (Basel) 10 (2020), https://doi.org/10.3390/met10081097.
[28] C. Moussa, M. Bernacki, R. Besnard, N. Bozzolo, About quantitative EBSD analysis of deformation and recovery substructures in pure Tantalum, in: IOP Conf. Ser. Mater. Sci. Eng, 2015, p. 89, https://doi.org/10.1088/1757-899X/89/1/012038.
[29] T.R. Smith, J.D. Sugar, C. San Marchi, J.M. Schoenung, Strengthening mechanisms in directed energy deposited austenitic stainless steel, Acta Mater. 164 (2019) 728–740, https://doi.org/10.1016/j.actamat.2018.11.021.
[30] S. Baraldo, A. Vandone, A. Valente, E. Carpanzano, Closed-Loop Control by Laser Power Modulation in Direct Energy Deposition Additive Manufacturing, in: Proc. 5th Int. Conf. Ind. 4.0 Model Adv. Manuf, 2020, pp. 15–58, https://doi.org/10.1007/978-3-030-46212-3_9.
[31] F. Bachmann, R. Hielscher, H. Schaeben, Texture analysis with MTEX- Free and open source software toolbox, Solid State Phenom 160 (2010) 63–68, https://doi.org/10.4028/www.scientific.net/SSP.160.63.
[32] L. Chechik, N.A. Boone, L.R. Stanger, P. Honniball, F. Freeman, G. Baxter, J. R. Willmott, I. Todd, Variation of texture anisotropy and hardness with build parameters and wall height in directed-energy-deposited 316L steel, Addit. Manuf. 38 (2021), 101806, https://doi.org/10.1016/j.addma.2020.101806.
[33] J.C. Stinville, C. Tromas, P. Villechaise, C. Templier, Anisotropy changes in hardness and indentation modulus induced by plasma nitriding of 316L polycrystalline stainless steel, Scr. Mater. 64 (2011) 37–40, https://doi.org/10.1016/j.scriptamat.2010.08.058.
[34] Grain Orientation Parameters, MTEX, 2022 n.d, https://mtex-toolbox.github.io/GrainOrientationParameters.html. accessed June 10.
[35] D. Rosenthal, The Theory of Moving Sources of Heat and Its Application to Metal Treatments, Trans. Am. Soc. Mech. Eng. 43 (1946) 849–866.
[36] M. Gäumann, C. Bezençon, P. Canalis, W. Kurz, Single-crystal laser deposition of superalloys: Processing-microstructure maps, Acta Mater. 49 (2001) 1051–1062, https://doi.org/10.1016/S1359-6454(00)00367-0.
[37] A.S. Agazhanov, D.A. Samoshkin, Y.M. Kozlovskii, Thermophysical properties of Inconel 718 alloy, J. Phys. Conf. Ser. (2019) 1382, https://doi.org/10.1088/1742-6596/1382/1/012175.
[38] P. Nie, O.A. Ojo, Z. Li, Numerical modeling of microstructure evolution during laser additive manufacturing of a nickel-based superalloy, Acta Mater 77 (2014) 85–95, https://doi.org/10.1016/j.actamat.2014.05.039.
[39] I.L. Svetlov, N.V Petrushin, D.V Shchegolev, K.K. Khvatskiy, Anisotropy of Mechanical Properties of Single Crystal in Fourth Generation Ni-Based Superalloy, in: 9th Liege Conf. Mater. Adv. Power Eng. 2010, 2010, pp. 1–6. https://www.osti.gov/etdeweb/servlets/purl/21588215.
[40] J.R. Cahoon, W.H. Broughton, A.R. Kutzak, The determination of yield strength from hardness measurements, Metall. Trans. 2 (1971) 1979–1983, https://doi.org/10.1007/BF02913433.
[41] M.O. Lai, K.B. Lim, On the prediction of tensile properties from hardness tests, J. Mater. Sci. 26 (1991) 2031–2036, https://doi.org/10.1007/BF00549163.